Miura et al. *NPG Asia Materials* (2022) 14:85
https://doi.org/10.1038/s41427-022-00432-1

NPG Asia Materials

ARTICLE Open Access

Thermodynamic approach for enhancing superconducting critical current performance

Masashi Miura[1,2,3], Go Tsuchiya[1], Takumu Harada[1], Keita Sakuma[1], Hodaka Kurokawa[4], Naoto Sekiya[5], Yasuyuki Kato[6], Ryuji Yoshida[7], Takeharu Kato[7], Koichi Nakaoka[8], Teruo Izumi[8], Fuyuki Nabeshima[4], Atsutaka Maeda[4], Tatsumori Okada[9], Satoshi Awaji[9], Leonardo Civale[2] and Boris Maiorov[2]

Abstract

The addition of artificial pinning centers has led to an impressive increase in the critical current density (J_c) of superconductors, enabling record-breaking all-superconducting magnets and other applications. The J_c of superconductors has reached ~0.2–0.3 J_d, where J_d is the depairing current density, and the numerical factor depends on the pinning optimization. By modifying λ and/or ξ, the penetration depth and coherence length, respectively, we can increase J_d. For $(Y_{0.77}Gd_{0.23})Ba_2Cu_3O_y$ ((Y,Gd)123), we can achieve this by controlling the carrier density, which is related to λ and ξ. We can also tune λ and ξ by controlling the chemical pressure in Fe-based superconductors, i.e., $BaFe_2(As_{1-x}P_x)_2$ films. The variation in λ and ξ leads to an intrinsic improvement in J_c via J_d, allowing extremely high values of J_c of 130 MA/cm^2 and 8.0 MA/cm^2 at 4.2 K, consistent with an enhancement in J_d of a factor of 2 for both incoherent nanoparticle-doped (Y,Gd)123 coated conductors (CCs) and $BaFe_2(As_{1-x}P_x)_2$ films, showing that this new material design is useful for achieving high critical current densities in a wide array of superconductors. The remarkably high vortex-pinning force in combination with this thermodynamic and pinning optimization route for the (Y,Gd)123 CCs reached ~3.17 TN/m^3 at 4.2 K and 18 T (**H**||*c*), the highest values ever reported for any superconductor.

Introduction

High-temperature superconductors are attractive because their high critical temperature (T_c) enables them to be used at high temperature and outperform standard superconductors in terms of magnetic field performance[1,2]. However, the limiting factor is the ability to arrest the motion of Abrikosov vortices at a very high critical current. The dissipative motion of vortices can be reduced or eliminated by pinning at nonsuperconducting defects. There are several possible approaches for enhancing the critical current density. Over the last three decades, enormous improvements in the properties of the oxide high-temperature superconductors (HTSs) of the $REBa_2Cu_3O_y$ family (RE123) have mostly been achieved by adding and tailoring pinning centers to immobilize vortices. The number of routes for engineering the pinning landscape to increase J_c is too large to describe and continues to be fruitful[3–12]. The creep-free J_c, $J_{c0,cal}^{NPs}(T,H)$, for strong pinning by nanoparticles ($D_{np} \geq 2\xi_{ab}$) is expressed as[11]

$$J_{c0}^{NPs} \propto N_{np}\frac{\mu_0 H_c^2 \pi \xi^2 D}{4\xi} \propto N_{np}\left(\frac{1}{\lambda^2 \xi}\right) \quad (1)$$

where N_{np} is the density of the nanoparticles (NPs), D is the mean size of the NPs, ξ_{ab} is the coherence length, λ_{ab} is the London penetration depth, and H_c is the thermodynamic critical field (see SI, Section 1). How close J_c can be to the upper limit of J_c, i.e., the depairing current density (J_d), by the addition of pinning centers is

Correspondence: Masashi Miura (masashi-m@st.seikei.ac.jp)
[1]Graduate School of Science and Technology, Seikei University, 3-3-1 Kichijoji-kitamachi, Musashino-shi, Tokyo 180-8633, Japan
[2]Materials Physics and Applications Division, Los Alamos National Laboratory, Los Alamos, NM 87545, USA
Full list of author information is available at the end of the article

still an open question. The J_d within the Ginzburg-Landau theory[13] is

$$J_d(T) = \frac{2\sqrt{2}H_c(T)}{3\sqrt{3}\lambda_{ab}(T)} = \frac{\phi_0}{3\sqrt{3}\pi\mu_0\lambda_{ab}(T)^2\xi_{ab}(T)} \propto \left(\frac{1}{\lambda^2\xi}\right) \quad (2)$$

where ϕ_0 is the flux quantum.

Experimentally, the enhancement in J_c by tuning the carrier density, especially in standard RE123 films, i.e., without artificial pinning centers (APCs), has been reported[14–16]. Recently, A. Stangl et al. reported that overdoped standard Y123 films grown by pulsed laser deposition (PLD) attained 18% J_d at 5 K, which is a consequence of the increase in condensation energy with charge carrier density[17]. On the other hand, by adding and tailoring APCs, the highest J_c achieved for RE123 and Fe-based films is in the range of 10–20% J_d[4–6,8–13]. Most of the studies introducing APCs into RE123 are on coherent $BaMO_3$ (BMO, M = Zr, Hf, Sn, etc.) nanorods[4,6,7,9,13] and coherent Y_2BaCuO_5 precipitates[5,10]. The *c* axis of the RE123 matrix is expanded by coherent APCs[7,11], resulting in a reduced carrier density due to strain-induced oxygen-vacancy formation and decreased crystallinity[6,7,11]. On the other hand, we have succeeded in introducing incoherent BMO NPs into not only $(Y_{0.77}Gd_{0.23})Ba_2Cu_3O_y$ ((Y,Gd)123) films[11] but also Fe-based pnictide $BaFe_2(As_{1-x}P_x)_2$ (Ba122:P) films[8], which leaves the matrix unaltered with just slightly decreased superconducting properties. The $BaHfO_3$ (BHO) NPs in RE123 films and $BrZrO_3$ (BZO) NPs in Ba122:P films have an average size ($D_{ave.}$) of 7 nm with a density $N_{np} \sim 80 \times 10^{21}$ m^{-3} and $D_{ave.}$ of 8 nm with $N_{np} \sim 68 \times 10^{21}$ m^{-3}, respectively. For both nanocomposite materials, we have shown a large enhancement in J_c at not only self-field but also in-field by introducing a high density of incoherent NPs of a tailored size[8,11]. Theoretically, using the time-dependent Ginzburg-Landau equations (TDGL) and a *targeted evolution* approach, Sadovskyy et al.[17] explored the optimization of J_c, showing that a level of 30–40% J_d could be attained.

Now, in addition to focusing on improving the pinning morphology, we can increase J_d. Considering Formulas (1) and (2), we see that $J_c \propto \left(\frac{1}{\lambda^2\xi}\right) \propto J_d$. Therefore, reducing ξ or λ would improve J_d and consequently J_c. However, these parameters are material-specific and have not been thoroughly studied for improving the J_c of APC-doped cuprates and Fe-based superconducting films. If both these characteristic lengths can be changed, in addition to the enhancement in the flux pinning, J_c can be dramatically improved through the enhancement in J_d. Increasing T_c has been the empirical method for increasing J_d; however, this depends on discovering new superconductors, and even in the cases where this has been achieved (e.g., $HgBa_2Ca_2Cu_3O_{8+\delta}$ and $Bi_2Sr_2Ca_2Cu_3O_{10+\delta}$), it has not led to improved performance, as the gains have been negated by the enhancement in thermal fluctuations that grow, since[3,18]

$$G_i^{1/2} \propto \left(T_c^2\gamma^2\lambda^4/\xi^2\right)^{1/2} \quad (3)$$

where G_i is the Ginzburg number.

Herein, we present a novel route for improving the performance of superconductors by increasing J_d. Unlike the increase in pinning, which is extrinsic, this route is thermodynamic: J_d is raised by decreasing λ and/or increasing $H_c \propto (\lambda\xi)^{-1}$ [14]. This method is general and applicable to any superconductor; herein, we show results for RE123 and Ba122:P films both with and without incoherent BMO NPs. The method works in conjunction with any pinning landscape improvement that has already been achieved, facilitating a method for increasing performance independent from the microstructure. As a concomitant advantage, the decrease in λ also reduces the deleterious effects of thermal fluctuations by reducing G_i. In the RE123 compounds, we achieve this by increasing the carrier concentration, and thus decreasing λ; we also detect an increase in H_c and a decrease in γ observed through the increased H_{c2} (i.e., decrease in ξ) with a consequent reduction in γ. When we combine this new strategy with our previously developed methods to incorporate a large density N_{np} of incoherent BHO NPs of a tailored size, we obtain $J_c \sim 150$ MA/cm^2 (~32.4% of J_d) and $J_c \sim 130$ MA/cm^2 (~28% of J_d) at 4.2 K and self-field for nanocomposite (Y,Gd)123 films on single-crystal substrates and metallic substrates (coated conductors), respectively. These improvements carry over to the *in-field* properties. We also apply this route in Ba122:P films with incoherent BZO NPs, where we can increase J_d and J_c by controlling λ and γ through the tuning of the chemical pressure. This coordinated strategy can inform the improvement efforts in the newly discovered hydrogen-based superconductors.

We start by increasing J_d by decreasing λ and ξ for RE123. The Cu-O planes containing chains in RE123 are an exception among other cuprates ($La_{2-x}Sr_xCuO_4$[19], $Y_{1-x}Cu_xSr_2Cu_2Tl_{0.5}Pb_{0.5}O_7$[20], $Tl_2Ba_2CuO_{6+x}$[21,22]) or Fe-pnictides[18]. This allows a unique opportunity for λ to be decreased[23] and H_c to be increased[24] up to the highest possible overdoping, unlike other cuprates[21,25] and Fe-pnictides[26] for which λ is minimized at the optimum T_c doping. An indication of the possible gain in terms of enhancing J_d by tuning the carrier concentration is observed in the specific heat jump (directly related to H_c) that for $y = 7$ ($p = 0.19$) is 45% higher than for optimum doping. These beneficial effects outweigh the negative effects of the 4% decrease in T_c. Thus, we proceed to

Table 1 Structural and superconducting properties.

Materials	p	T_c [K]	$\gamma = H_{c2}^{ab}/H_{c2}^{c}$	$\mu_0 H_{c2}^{cal}(0)$ [T]	$\xi_{ab}(0)$ [nm]	$\lambda_{ab}(0)$ [nm]	$\mu_0 H_c^{cal}(0)$ [T]	$J_d(0)$ [MA/cm^2]
(Y,Gd)123 CCs	0.177 ($T_A = 300$ °C)	90.2	4.7	119.1 ± 1.8	1.66	114	1.23	466.61
	0.160 ($T_A = 450$ °C)	92.2	5.4	86.4 ± 1.4	1.95	129	0.92	310.37
	0.142 ($T_A = 500$ °C)	89.8	5.8	58.4 ± 0.9	2.37	145	0.68	201.97
(Y,Gd)123 + BHO CCs	0.18 ($T_A = 300$ °C)	89.2	4.3	126.5 ± 1.4	1.61	112	1.29	498.02
	0.168 ($T_A = 450$ °C)	91.7	4.7	97.0 ± 0.8	1.84	122	1.04	367.68
	0.144 ($T_A = 500$ °C)	90.2	5.5	72.0 ± 1.6	2.14	143	0.76	230.57

$\mu_0 H_{c2}(0)$, $\xi_{ab}(0)$, $\lambda_{ab}(0)$ and J_d for the (Y,Gd)123 and (Y,Gd)123 + BHO CCs at different p. Error bars on $\mu_0 H_{c2}(0)$ were determined from the uncertainty in the corresponding data analysis.

change the oxygen content y and modify the carrier concentration p to ultimately change λ and ξ for RE123 with two very different pinning landscapes. In Table 1, we summarize the main experimental results for the RE123 compounds. To avoid changes stemming from different T_c values, we compare two samples with similar T_c (89.2 and 90.2 K) that are on either side of the optimal doping, i.e., $p = 0.18$ and 0.144. A comparison of these samples leads to J_d values of 498 and 230 MA/cm^2, respectively, almost an increase by a factor of two with decreases in λ and ξ.

Materials and methods

Film growth

The epitaxially grown Y123 nanocomposite films of standard (Y,Gd)123 and BHO NP-doped (Y,Gd)123 ((Y,Gd)123 + BHO) films were grown from metal organic solutions including Y-, Gd-, and Ba-trifluoroacetates and Cu-naphthenate with a cation ratio of 0.77:0.23:1.5:3 on buffered tapes of CeO_2 (grain-boundary angles, $\Delta\phi_{ceo2} = 3.0°$)/Y_2O_3/$LaMnO_3$/ion-beam-assisted deposition (IBAD)-MgO/$Gd_2Zr_2O_7$/Hastelloy C276 (Haynes International Inc., Kokomo, IN, USA). We added Hf-naphthenate into the (Y,Gd)123 solutions; the volume percent of BHO was 12, and the concentration of the starting solution was 0.45 mol/L with a coating thickness (d_{coat}) of 30 nm, resulting in small-size (7 nm) and high-density (7.5×10^{22} m^{-3}) nanoparticles while maintaining the crystallinity and T_c of the RE123 matrix. Moreover, nanocomposite ((Y,Gd)123 + BHO) films were also fabricated on $CeO_2(\Delta\phi_{CeO2}(220) = 1.0°)$/R-$Al_2O_3$ single-crystals. For comparison, we also fabricated 10 mol.% BHO-doped Eu123 (Eu123 + BHO) films on buffered tapes of CeO_2 ($\Delta\phi_{CeO2}(220) = 3.0°$)/$Y_2O_3$/$LaMnO_3$/ion-beam-assisted deposition (IBAD)-MgO/$Gd_2Zr_2O_7$/Hastelloy C276. The Eu123 + BHO film exhibited coherent BHO nanorods of 5 nm diameter, not incoherent BHO NPs, which are obtained with metal organic deposition (MOD). The details of the PLD film preparation have been published elsewhere[27]. The total thickness of the RE123 layer for all samples was 600 nm to 1000 nm, which was confirmed by cross-sectional transmission electron microscopy (TEM, JEM-F200, JEOL Ltd., Tokyo, Japan). The standard $BaFe_2(As_{1-x}P_x)_2$ and 3 mol. % $BaZrO_3$ (BZO)-doped epitaxial films were deposited on MgO (100) single-crystal substrates by ablating the polycrystalline pulsed laser deposition targets using the second harmonic (wavelength: 532 nm) of a pulsed Nd:YAG laser at a repetition rate of 10 Hz in a vacuum of 10^{-4} Pa at a substrate temperature of 850 °C. In this work, the amount of P substitution x in the target was selected as 0.33, 0.40, and 0.50. The total thickness of the (Ba122:P) films with and without BZO was 80 nm.

Oxygenation treatments for cuprate films

The oxygenation treatments were precisely controlled to tune the carrier concentration for the (Y,Gd) 123 + BHO coated conductors (CCs). The oxygenation process is reversible, as confirmed by the ability to recover $T_{c,zero}$ and $J_c^{s.f.}$ after varying the oxygen content (SI, Fig. S1 and Table S1). In an investigation of bulk RE123 (RE = Nd, Sm, Eu, Gd Dy, Ho and Y), the optimum doping annealing temperature ($T_A^{opt.}$) was found to depend on the RE element[28]. For maximum T_c, RE123 with larger RE^{3+} ions required lower O_2 annealing temperatures compared to RE123 with smaller RE^{3+} ions (at the same O_2 pressure). $T_A^{opt.}$ (the temperature for the highest $T_{c,zero}$ and smallest ΔT ($= T_{c,onset} - T_{c,zero}$) for each RE123 material) for our RE123 CCs prepared by different growth methods (MOD and PLD) is consistent with that of bulk studies[28], at $T_A^{opt.} = 500$, 450 and 350 °C for Y123, (Y,Gd)123 and Eu123 CCs, respectively (See SI, Fig. S2). In this work, for the oxygenation of the RE123 films prepared from different fabrication processes (MOD and PLD), we annealed in an O_2 environment of 1.1 atm, and each annealing temperature ($T_A = 300$–550 °C) was held for 3 h and then rapidly quenched to room temperature. From the c-axis length

measured by XRD (RINT2100 and ATX-G (Rigaku Co., Tokyo, Japan)) and $T_{c,zero}$, annealing at 300 °C for 3 h was sufficient to oxygenate the RE123 films.

Transport properties in magnetic fields

The films were patterned using a pulsed fiber laser (1095 nm, 20 W) into bridges of ~50 μm width. The crystalline quality was examined by X-ray diffraction (XRD). The temperature dependence of the resistivity (ρ) was measured by a four-probe method in the temperature range of 4–300 K using a physical property measurement system (PPMS, Quantum Design, Inc., San Diego, CA, USA) with a superconducting magnet generating a field H up to 14 T and in an 18 T-superconducting magnet at Tohoku University. In the PPMS, a rotational stage was used to rotate the samples with respect to H. The critical current was determined using a 1 μV cm^{-1} criterion. H_{c2} and H_{irr} were determined using 0.90 ρ_N and 0.01ρ_N criteria, respectively, where ρ_N is the normal-state resistivity. Hall measurements were conducted in a magnetic field of 9 T. The six electrical contacts used silver paste on silver pads deposited on the film by sputtering. The magnetization studies were performed using a SQUID (Quantum Design, Inc., San Diego, CA, USA) magnetometer to characterize the temperature and field dependence of J_c and S.

Results

Controlling the carrier density of the superconducting films

First, to investigate the effects of introducing coherent BHO nanorods on the $T_{c,zero}$, c-axis length and self-field J_c ($J_c^{s.f.}$), we measured the hole concentration (n_H, determined from the Hall effect at 300 K) dependence of these properties for both standard Eu123 and Eu123 with coherent BHO nanorod (Eu123 + coherent BHO) CCs grown by PLD (Fig. 1a, b). $T_{c,zero}$ is determined using a 0.01ρ_N criterion. As shown in the inset of Fig. 1a, the Eu123 + coherent BHO CC has coherent BHO nanorods with a diameter of 5 nm. As shown in Fig. 1a, the $T_{c,zero}$ and c-axis length of the standard Eu123 CCs decrease systematically with decreasing oxygenation temperature (T_A) from ${n_H}^{300K} = 9.4 \times 10^{21}/cm^3$ (optimum doped) to $15.3 \times 10^{21}/cm^3$, confirming that the samples are in the overdoped regime. On the other hand, although the Eu123 + coherent BHO CCs are treated under the same O_2 annealing conditions as the overdoped standard CCs, $T_{c,zero}$ is not reached even for the optimum doping level (i.e., underdoped regime), and the c-axis length is longer than that in standard Eu123 CCs. Figure 1b shows $J_c^{s.f.}$ as a function of carrier concentration (doping level) in the CuO_2 layer (p) for both the standard Eu123 and Eu123 + coherent BHO CCs. The variation in p is determined by following $T_{c,zero}$ on the universal doping curve[29], where $T_{c,zero}$ reaches its maximum at optimum doping ($p = 0.16$) (see Supplementary Information, Fig. S3). As a result, although the Eu123 + coherent BHO films have strong pinning, the $J_c^{s.f.}$ of the nanocomposite CCs is not enhanced compared to that of the standard ones because the carrier concentration p is lower due to the strain-induced oxygen-vacancy formation, leading to a reduction in the carrier doping level[7]. There are no reports of overdoped RE123 with coherent APCs because it is generally difficult to overdope coherent APC-doped RE123 films, although overdoping is easily achieved in standard films (with no APCs).

Now, we focus on our incoherent BHO NP-doped (Y,Gd)123 CCs. As shown in Fig. 1c, although the (Y,Gd)123 + BHO CCs have a high density of NPs (see inset of Fig. 1c), $T_{c,zero}$ and the c-axis length systematically decrease with decreasing oxygenation temperature (T_A) from ${n_H}^{300K} = 9.4 \times 10^{21}/cm^3$ (optimum doped) to $21 \times 10^{21}/cm^3$, attaining overdoped status. However, the $J_c^{s.f.}$ at 77 K (see Fig. 1d) increases monotonically with increasing p beyond optimum doping. Even though the (Y,Gd)123 and (Y,Gd)123 + BHO CCs have almost the same $T_{c,zero}$-n_H broad peak (because the superconducting matrix remains intact[11]), the $J_c^{s.f.}$ of the (Y,Gd)123 + BHO CC is over two times higher than that of the (Y,Gd)123 CC. It is worth noting that even though $T_{c,zero} \sim 90$ K is almost the same for the (Y,Gd)123 + BHO CCs with ${n_H}^{300K} = 7 \times 10^{21}/cm^3$ and ${n_H}^{300K} = 21 \times 10^{21}/cm^3$, as shown in Fig. 1c, the overdoped CC shows a $J_c^{s.f.}$ 1.8 times higher at 77 K. It is worth noting that we achieved an overdoped doping level up to $p = 0.18$ for our incoherent BHO NP-doped (Y,Gd)123 CCs but not for the standard one (without APCs).

Influence of grain boundaries in carrier density-controlled films

To clarify that the enhancement in J_c (Fig. 1d) for our overdoped (Y,Gd)123 + BHO CCs, which are fabricated on oxide-buffered metallic substrates (in-plane crystallinity ($\Delta\phi_{CeO2} = 3°$)), is not due to doping-induced improved grain-boundary properties (similar to the improvement in the intergrain-J_c for Ca-doped Y123 films on bicrystal substrates[30]), we investigated the in-plane crystallinity of CeO_2 ($\Delta\phi_{CeO2}$) buffered metallic substrates with respect to the self-field J_c at 77 K of underdoped (Y,Gd)123, underdoped (Y,Gd)123 + $BaHfO_3$ and overdoped (Y,Gd)123 + $BaHfO_3$ films (Fig. 2a). For $\Delta\phi_{CeO2} > 3°$, the $J_c^{s.f.}$ of all films decreases exponentially with increasing boundary angle. However, for $\Delta\phi_{CeO2} < 3°$, the $J_c^{s.f.}$ of all films decreases by just 10% when changing $\Delta\phi_{CeO2}$ from 0.6° to 3° independent of p and of the pinning landscape. As shown in Fig. 2b, although the ratio of $J_c^{s.f.}(\Delta\phi)/J_c^{s.f.}(0.6°)$ for $\Delta\phi_{CeO2} > 3°$ of the two underdoped films is lower than that of the overdoped film, the ratio for

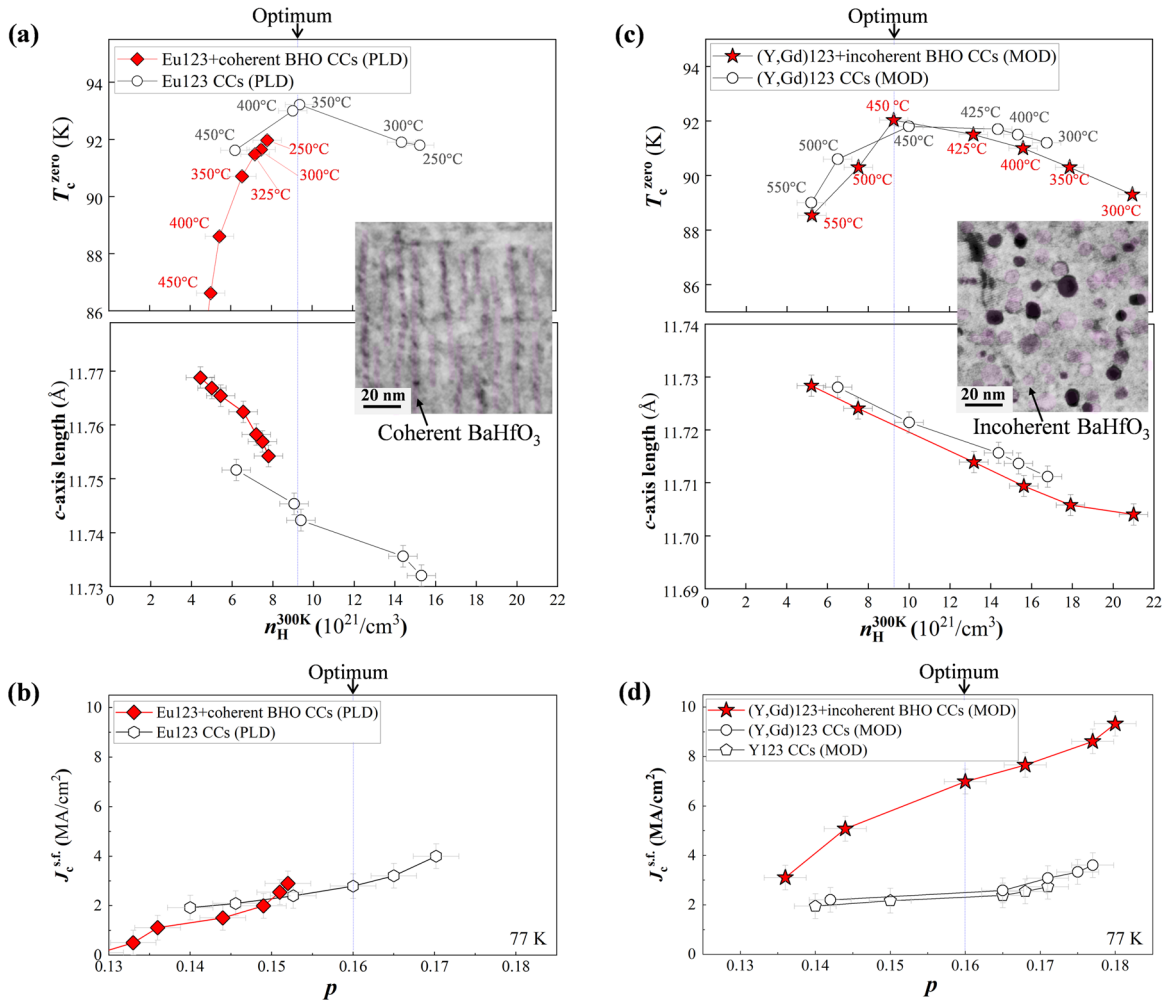

Fig. 1 Carrier concentration dependence *p* of critical temperature T_c, *c*-axis length and self-field critical current density $J_c^{s.f.}$. a Dependence of T_c (top panel) and *c*-axis length (bottom panel) on n_H at 300 K and **b** *p* dependence of $J_c^{s.f.}$ at 77 K for standard Eu123 and Eu123 + BHO CCs grown by PLD. **c** Dependence of T_c and *c*-axis length on n_H at 300 K (**d**) *p* dependence of $J_c^{s.f.}$ for standard (Y,Gd)123 and (Y,Gd)123 + BHO CCs grown by MOD. The insets of Fig.1a and c are cross-sectional TEM images of the Eu123 + BHO and (Y,Gd)123 + BHO CCs, where BHO NPs are colored. The error bars of J_c were determined from the uncertainty in the in-plane crystallinity, natural defects, and film thickness.

$\Delta\phi_{CeO2} < 3°$ clearly shows exactly the same trend even for different *p*-values (underdoped and overdoped) and for different microstructures (without and with BHO NPs). To investigate the GB misorientation angles in our MOD CCs, we studied the plan-view TEM images of (Y,Gd)123 CCs on $\Delta\phi_{CeO2} = 3°$ buffered metallic substrates (see inset of Fig. 2b). The chain of edge dislocation distances (D) is 13.5–15.3 nm for a film on $\Delta\phi_{CeO2} = 3°$, which represents the misorientation angles of 1.5–1.7° calculated using $D = (|b|/2)/\sin(\theta_{GB}/2)$, where $|b|$ is the norm of the corresponding Burgers vector. Because the crystal growth of MOD films is meandering and passes over the substrate grain boundaries (differing from that in PLD), the value of the misorientation angle is almost half that of $\Delta\phi_{CeO2}$, which is the same as the in-plane crystallinity of (Y,Gd)123 ($\Delta\phi_{(Y,Gd)123}(103) = 1.5°$), as evaluated by XRD. It is clear that the GBs of (Y,Gd)123 and (Y,Gd)123 + $BaHfO_3$ CCs grown on $\Delta\phi_{CeO2} = 3°$ of CeO_2 buffered metallic substrate are not Josephson weakly linked (i.e., with a locally suppressed order parameter). Based on Fig. 2a, b, we conclude that our $J_c^{s.f.}$ properties for films grown on $\Delta\phi_{CeO2} = 3°$ of CeO_2 buffered metallic substrates mainly depend on the value of the intragrain J_c, not the intergrain-J_c, as is the case for large misorientation angles of the GBs[30].

Penetration depth and coherence length in carrier-controlled films

In Fig. 3, we show that λ and ξ vary with carrier concentration (p). We observed changes consistent with those found in the literature for single-crystal samples. The upper panel of Fig. 3a presents the measured λ_{ab} as a

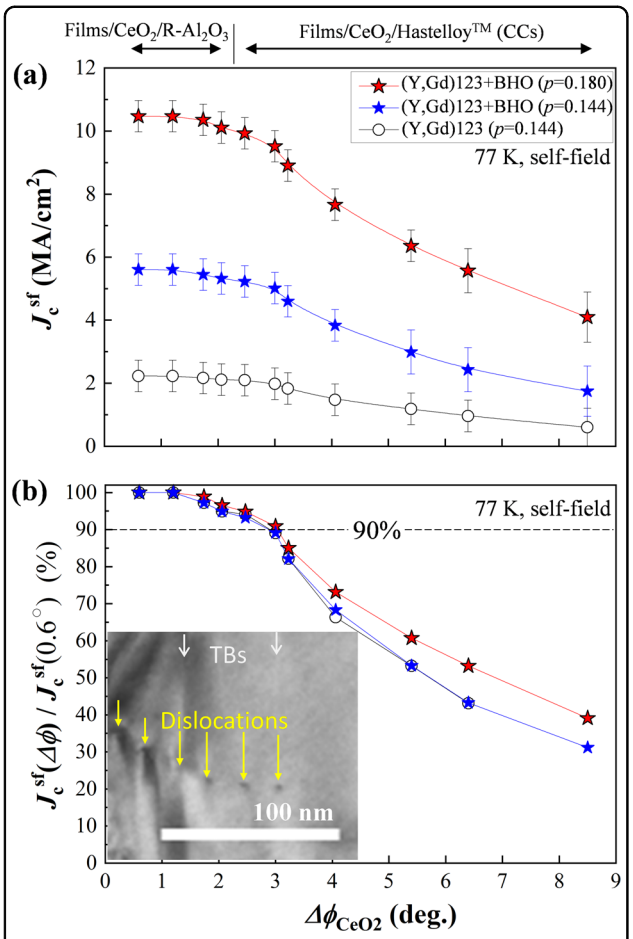

Fig. 2 Self-field critical current density $J_c^{s.f.}$ as a function of the in-plane crystallinity of the buffer layer ($\Delta\phi_{CeO2} = 3°$). a $J_c^{s.f.}$ and **b** the ratio $J_c^{s.f.}/J_c^{s.f.}$ ($\Delta\phi_{ceo2} = 0°$) at 77 K for the underdoped (Y,Gd)123, underdoped (Y,Gd)123 + $BaHfO_3$ and overdoped (Y,Gd)123 + $BaHfO_3$ films grown on CeO_2-buffered metallic substrates ($2.5° < \Delta\phi_{ceo2} < 8.5°$) and on CeO_2 buffered R-Al_2O_3 substrates ($0.6° < \Delta\phi_{ceo2} < 2°$). The inset of Fig. 2b shows the plane-view TEM image of the (a Y,Gd)123 film on a CeO_2 buffered metallic substrate with $\Delta\phi_{CeO2} = 3.0°$. White and yellow indicate the twin boundaries (TBs) and dislocations, respectively. The error bars of J_c were determined from the uncertainty in the in-plane crystallinity, natural defects and film thickness.

function of p for Y123[23,31] and (Y,Ca)123[32] single-crystals. For refs. [23,31], we calculated the penetration depth using $\lambda_{ab} = [\lambda_a\lambda_b]^{1/2}$. For the extraction of $\lambda_{ab}(0)$ for our (Y,Gd)123 + BHO film, we use the temperature dependence of the resonant frequency of the coplanar waveguide resonators based on the equations derived by K. Watanabe et al.[33] (measurement details are shown in SI, Figs. S4 and S5). Indeed, for $\lambda_{ab}(0)$, the decrease with increasing p for (Y,Gd)123 + BHO films is similar to that of Y123 and (Y,Ca)123 single-crystals[23,31,32].

The $H_{c2}(0)$ for $\mathbf{H}||c$ for the (Y,Gd)123 + BHO CCs with different p-values are shown in the lower panel of Fig. 3a. The values for (Y,Gd)123 + BHO CCs and Gd123 single-crystals are estimated by using the Werthamer–Helfand–Hohenberg (WHH) formula[34] (detailed data in SI, Figs. S6 and S7). The (Y,Gd)123 + BHO CCs with $p = 0.144$, 0.168 and 0.180 exhibit an upward trend in $H_{c2}(0)$ similar to that of Gd123 single-crystals (measured) and Y123 single-crystals from ref. [35]. The $\mu_0 H_{c2}{}^c(0)$ vs. p trend for our (Y,Gd)123 + BHO CCs and the Gd123 single-crystal is consistent with Y123 single-crystal studies, showing that H_{c2} increases with p up to $p = 0.18$.

Using λ_{ab} (upper panel of Fig. 3a) and ξ_{ab}, we calculated $H_c(0)$ using $\mu_0 H_c(0) = \frac{\phi_0}{2\sqrt{2}\pi\lambda_{ab}(0)\xi_{ab}(0)}$ for our (Y,Gd)123 + BHO films and Y123 single-crystals[23,31,35] with various p-values, as shown in the upper panel of Fig. 3b. These results are consistent with the calculated $H_c(0)$ values based on H_{c2} and H_{c1} for the Gd123 single-crystal (detailed data in SI, Fig. S7). The $H_c(0)$ values for the (Y,Gd)123 + BHO CCs increase with increasing p, which is a similar trend to that for the Gd123 and Y123 single-crystals.

In view of the changes in ξ and λ, summarized in Table 1, we can use $J_d \propto \left(\frac{1}{\lambda^2\xi}\right)$ and assert that the variation in λ is more important for J_d than the variation in ξ, as λ also affects H_c. The enhanced H_c is one of the main reasons for the higher J_c of our most overdoped (Y,Gd)123 + BHO film with $p = 0.18$ and the J_c calculated for strong pinning nanoparticle-doped films, $J_{c0,cal}^{NPs} \propto \left(\frac{1}{\lambda^2\xi}\right)$ (see Supplementary Information, Section 9). The monotonic increase in $H_c(0)$ with p shown in the upper panel of Fig. 3b, consistent with previous studies in single-crystal[36] and polycrystalline[24] Y123, confirms the different behavior of Y123 compared to other HTS cuprate materials where $H_c(0)$ and $\Delta C/T_c$ coincide with the maximum of T_c[20,22].

To investigate the n_s dependence of the normal-state carrier density for Y123, we calculated n_s for (Y,Gd)123 + BHO CCs with different p. The dependence of the effective mass (m^*) in Y123 single-crystals on the hole doping level was recently measured[37]. To calculate the n_s for our (Y,Gd)123 + BHO CCs, we used the relationship $\lambda_{ab}(0) = \sqrt{\frac{m^*}{\mu_0 n_s(0) e^2}}$ and m^* from reference[37] (no m^* data above $p = 0.152$ was reported, so we extrapolated from the available curve). The n_s for our (Y,Gd)123 + BHO CCs increases monotonically with the hole concentration, as shown in the lower panel of Fig. 3b. This is consistent with the Y123 single-crystal data, also shown for comparison[23,31].

As shown in Fig. 3, the overdoped (Y,Gd)123 + BHO CCs have larger H_c and smaller λ_{ab} than the under—and optimally doped CCs, indicating an increase with p of J_c ($\propto \lambda^{-2}\xi^{-1}$) and J_d ($\propto\lambda^{-2}\xi^{-1}$). From Formula (1), the

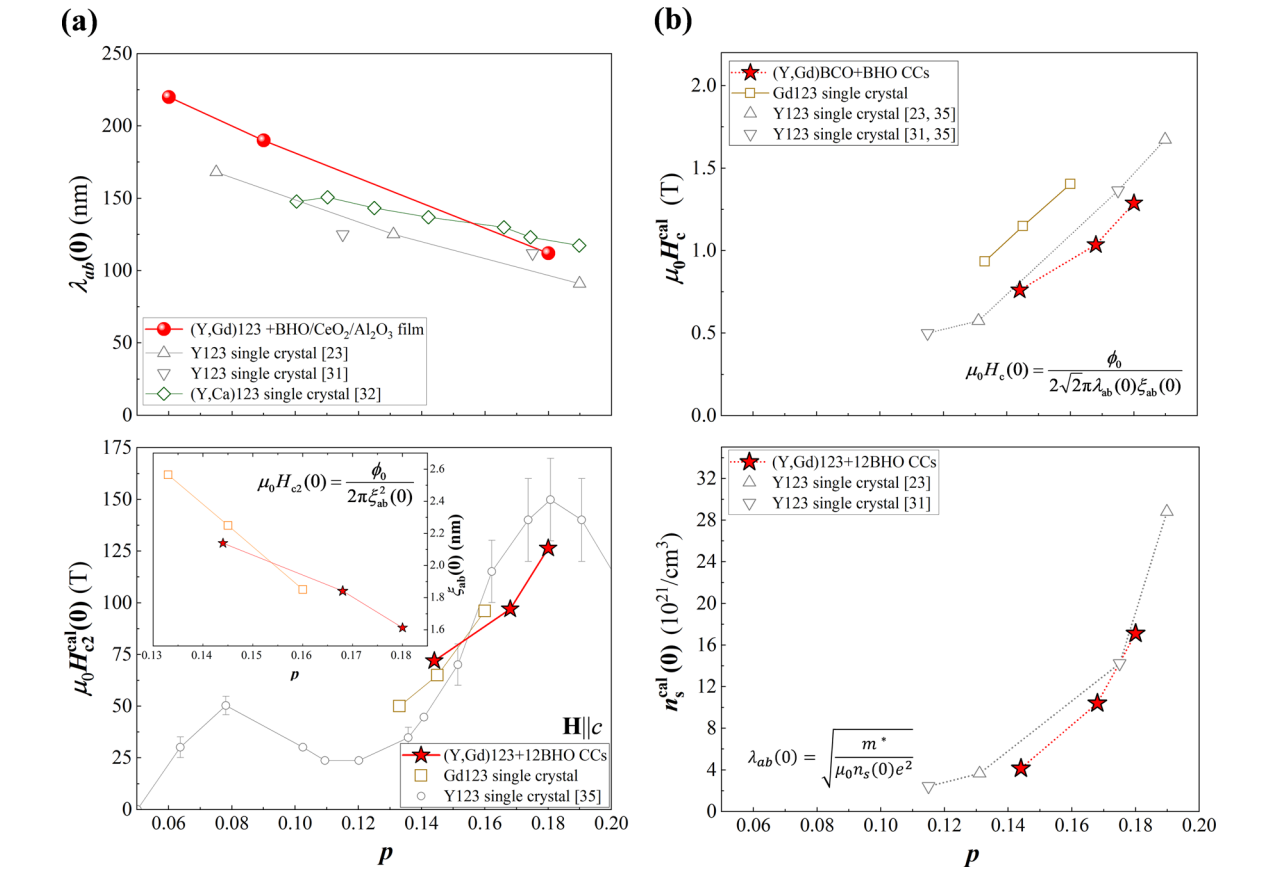

Fig. 3 Carrier concentration dependence *p* of penetration depth λ_{ab}, upper critical field $H_{c2}(0)$, thermodynamic critical field $H_c(0)$ and superfluid density $n_s(0)$. a λ_{ab} (upper panel) and $H_{c2}(0)$ estimated by using WHH (lower panel) as a function of carrier concentration (*p*) for the (Y,Gd)123 + BHO films. **b** Calculated $H_c(0)$ from Formula (3) (upper panel) and estimated superfluid density (lower panel) as a function of *p* for our (Y,Gd)123 + BHO CCs. For reference, values for Y123[23,31,35] and (Y,Ca)123[32] single-crystals are also shown. The error bars of $H_{c2}(0)$ for the Y123 single-crystal[35] are reported values, which represent the uncertainty in extrapolating $H_{c2}(T)$ to $T = 0$.

(Y,Gd)123 + BHO CCs with $p = 0.144$, 0.168 and 0.180 yield $J_d(0) = 230$, 368 and 498 MA/cm^2, respectively. This remarkable enhancement in the $J_d(0)$ of the overdoped sample is due to the reduced $\xi_{ab}(0)$ and $\lambda_{ab}(0)$ achieved by controlling the carrier density.

Substantially higher J_c at all temperatures

Consistent with the enhancements in J_c being induced by the changes in J_d, we observed the same enhancement at all temperatures over a wide range of applied magnetic fields. The upper panel of Fig. 4a shows the calculated $J_d(T)$ with different *p* based on the parameters in Table 1. The overdoped (Y,Gd)123 + BHO CC ($p = 0.18$) has a higher $J_d(T)$ than films with $p = 0.168$ and 0.144. As seen in the lower panel of Fig. 4a, the $J_d(T)$ for $p = 0.18$ is ~2 times higher than that for $p = 0.144$ over a wide temperature range. Figure 4b shows $J_c^{s.f.}(T)$ for the (Y,Gd)123 + BHO CCs with different *p*. Even though all the CCs have the same high density of BHO nanoparticles, $J_c^{s.f.}$ for $p = 0.18$ is the highest at all temperatures. Although CCs with $p = 0.18$ and $p = 0.144$ have almost the same T_c, slightly lower than that for the optimum doped one, the $J_c^{s.f.}$ of the $p = 0.18$ film is almost twice that of $p = 0.144$. At $p = 0.18$, the $J_c^{s.f.}$ for the (Y,Gd)123 + BHO CC achieves a maximum value of 130 MA/cm^2 at 4.2 K. This is higher than that previously reported for any superconducting material[6,9,11,13,17,38] except nanowires and ultrathin films (where the flux pinning mechanism is different)[39–41]. The $J_c^{s.f.}$ results are independent of the sample's width (*W*) and length (*L*), as demonstrated by the results at 77 K (SI, Fig. S8), indicating very uniform superconducting films. If we apply our finding to a film on a CeO_2 ($\Delta\phi_{ceo2} = 1°$) buffered R-Al_2O_3 single-crystal (shown in the inset of Fig. 4b), we achieve a $J_c^{s.f.}$ of ~150 MA/cm^2 at 4.2 K, which is also the highest value ever reported for any superconducting material with a thickness >> λ_{ab}. The enhancement of 1.15 in $J_c^{s.f.}$ at 4.2 K for the film on a single-crystal substrate compared to the film on an oxide-buffered metallic substrate (all other parameters being the same) is almost

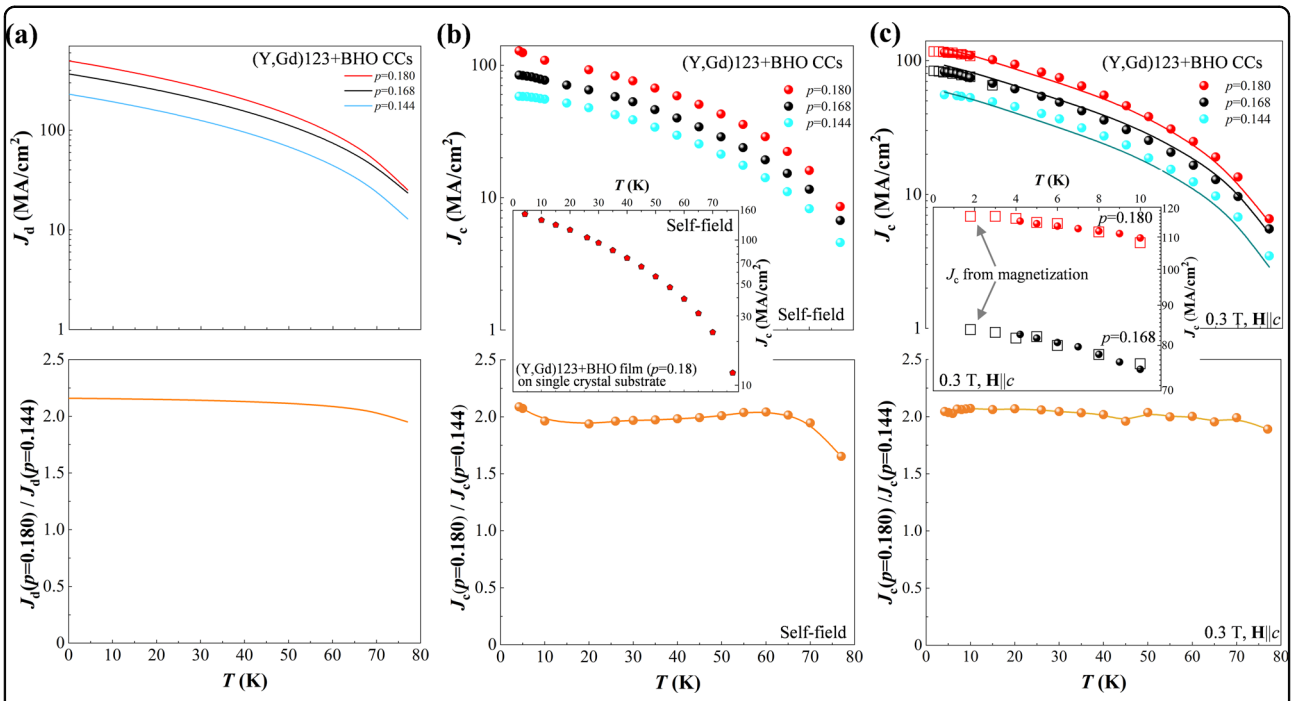

Fig. 4 Temperature dependence of critical current density J_c. a Calculated $J_d(T)$ for different p for the (Y,Gd)123 + BHO CCs based on the parameters in Table 1. **b** $J_c^{s.f.}(T)$ for the (Y,Gd)123 + BHO CCs with different p-values. The inset of Fig. 4b shows the $J_c^{s.f.}(T)$ for the (Y,Gd)123 + BHO ($p = 0.18$) film on CeO_2 buffered R-Al_2O_3 single-crystal substrate. **c** In-field $J_c(T)$ at $\mu_0 H = 0.3$ T and **H**||c for the (Y,Gd)123 + BHO CCs at various p. A comparison of transport J_c and J_c calculated from magnetization using the Bean model for the (Y,Gd)123 + BHO CCs is shown in the inset of Fig. 4c.

the same enhancement of 1.1 at 77 K (compared to the $J_c^{s.f.}$ of films on $\Delta\phi_{ceo2} = 1°$ and $\Delta\phi_{ceo2} = 1°$ of substrates in Fig. 2b) due to the slightly higher in-plane crystallinity of the former.

Insights into the benefit of further controlling J_d by changing the hole doping level are given by the in-field $J_c(T)$ at $\mu_0 H = 0.3$ T and H||c in Fig. 4c. The overdoped (Y,Gd)123 + BHO CC ($p = 0.18$) shows the highest in-field J_c, approximately twice the value for $p = 0.145$. As shown in the inset of Fig. 4c, the transport J_c coincides very well with the J_c calculated from magnetization (measured on a different piece) using the Bean model[42], indicating that our J_c values are highly uniform and reproducible. The solid lines in the upper panel of Fig. 4c are the calculated J_c ($J_{c0,cal}^{NPs}$)[3], and the solid symbols are the experimentally obtained parameters (calculation details are shown in Supplementary Information, Table S2), indicating that $J_{c0,cal}^{NPs}$ for (Y,Gd)123 + BHO CCs with different p are in good agreement with the experimental J_c. This agreement confirms the critical role of the decrease in λ and increase in H_c. The most interesting and important feature of the data presented here is that the enhancement ratios in J_d-T and J_c-T in both the self and in-field are identical (see lower panels of Fig. 4). This confirms that we can enhance J_c by enhancing J_d by changing H_c and λ while keeping the pinning enhancement intact.

Ginzburg number of carrier-controlled films

The top panel of Fig. 5a shows the γ values for (Y,Gd)123 and (Y, Gd)123 + BHO CCs with various hole concentrations measured at 300 K. The γ is calculated from the angular dependence of H_{c2} (see Supplementary Information, Fig. S9 and ref. [43] for details). For CCs both with and without BHO, the c-axis length (Fig. 1c) and mass anisotropy decrease with increasing n_H, i.e., hole doping level. These dependences follow the same trend observed in the c-axis length vs. p characteristics of the Y123 SC[44] and in the γ vs. p characteristics of the (Y,Ca)123 SC[45]. We also observed a systematic reduction in the c-axis length and smaller mass anisotropy for the samples with nanoparticles. The origin of this effect is under investigation and will be the focus of future publications.

As indicated above, the reduction in γ also diminishes the effect of thermal fluctuations, as characterized by $G_i \sim \gamma^2$ (see Formula (3)). While J_c increases by increasing J_d, it can also increase by reducing the effect of flux creep. The effect of flux creep is characterized by the creep rate, S, with which pinned vortices escape from the pinning

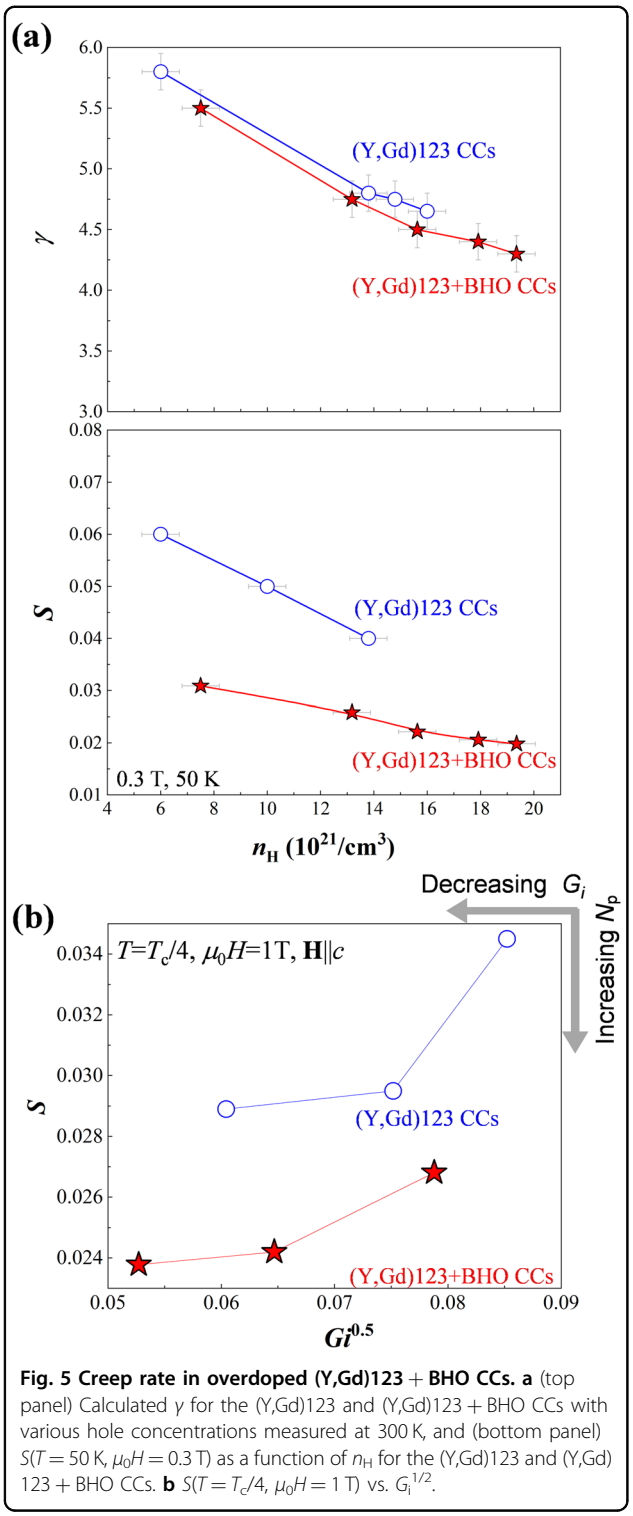

Fig. 5 Creep rate in overdoped (Y,Gd)123 + BHO CCs. a (top panel) Calculated γ for the (Y,Gd)123 and (Y,Gd)123 + BHO CCs with various hole concentrations measured at 300 K, and (bottom panel) $S(T = 50\,\text{K}, \mu_0H = 0.3\,\text{T})$ as a function of n_H for the (Y,Gd)123 and (Y,Gd)123 + BHO CCs. **b** $S(T = T_c/4, \mu_0H = 1\,\text{T})$ vs. $G_i^{1/2}$.

centers under thermal agitation. It was found that there is a universal lower limit of the creep rate $S_{min} \sim G_i^{1/2}(T/T_c)$[18], which demonstrates that the creep rate can be essentially reduced by reducing the anisotropy of the superconductor. In addition, S can also be reduced to its limit S_{min} by adding pinning.

The bottom panel of Fig. 5a shows $S(T = 50\,\text{K}, \mu_0H = 0.3\,\text{T})$ vs. n_H for our CCs, as a representative example of $S(T,H)$ over a wide range of conditions outside the Anderson-Kim (A–K) regime. This relationship can also be replotted as that of $S(T = T_c/4, \mu_0H = 1\,\text{T})$ (i.e., inside the A–K regime) vs. $G_i^{1/2}$ as shown in Fig. 5b. Thus, reducing the anisotropy is a new way to reduce S. In addition, the introduction of nanoparticles is effective, as seen from the comparison between (Y,Gd)123 + BHO CCs and (Y,Gd)123 CCs.

Discussion

The effect of J_d on J_c is general and apparent for different superconductors with varied pinning landscapes (see Fig. 6). Herein, we display $J_c^{s.f.}$ as a function of J_d at 4.2 K[43–52]. Details of the calculation parameters for J_d and experimentally obtained J_c are shown in SI, Table S3. First, we see that there is a general trend for several superconductors in which J_c is proportional to J_d (clearly seen in the inset of Fig. 6). Second, as shown in Fig. 6 for standard (Y,Gd)123 CCs, we can tune $J_c^{s.f.}$ at 4.2 K from 23.5 to 44.5 MA/cm^2 by changing J_d. We note that the relation of $J_c \sim 0.1J_d$ remains unchanged. Enhancements in J_d and J_c by tuning the carrier concentration are also observed for Ca-doped Y123 SC[50]. Third, the combination of controlling J_d by tuning the carrier concentration in a film with a high density of nanoparticles leads to the highest $J_c^{s.f.}(4.2\,\text{K}) = 130$ MA/cm^2 for (Y,Gd)123 + BHO CCs, which is 28.0% J_d. Moreover, a (Y,Gd)123 + BHO film on a single-crystal achieved 32.4% J_d ($J_c^{s.f.}(4.2\,\text{K}) = 150$ MA/cm^2) because of the further improvement obtained by the higher in-plane crystallinity. This value is close to the 33% achievement predicted by Gurevich[53] for a superconductor with NP pinning centers similar to the actual conditions in our (Y,Gd)123 + BHO films and CCs.

As shown in the inset of Fig. 6, increasing J_d is an effective method for enhancing J_c for not only Y123 cuprate CCs but also Fe-based pnictide Ba122:P films. In the Ba122:P system, the isovalent substitution of P for As induces chemical pressure, suppressing magnetism and inducing superconductivity, which is different from the effect of electron doping or hole doping[54–56]. For standard Ba122:P films, by tuning x, the $J_c^{s.f.}$ at 4.2 K increases from 1.0 to 3.6 MA/cm^2 due to the increase in J_d from 23 to 74 MA/cm^2. Moreover, Ba122:P + BZO films with different x show that J_c increases (up to 8 MA/cm^2 at 4.2 K) with increasing J_d, indicating that the combined approach of tuning J_d and enhancing flux pinning (i.e., adding NPs) can also be used to improve the performance of superconductors of different families. In this

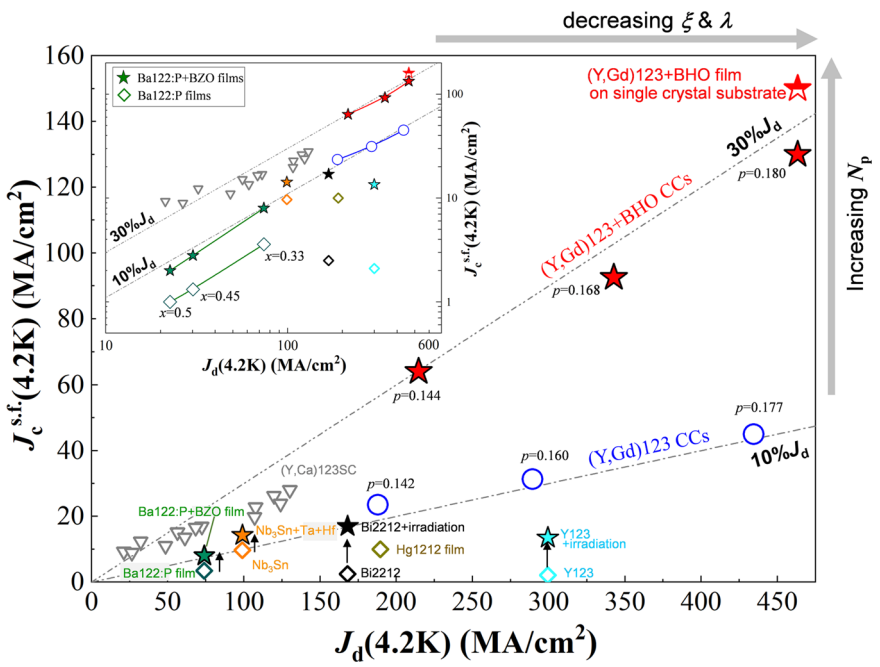

Fig. 6 Self-field critical current density $J_c^{s.f.}$ v.s. depairing current density J_d for various superconducting materials. $J_c^{s.f.}$ at 4.2 K as a function of J_d at 4.2 K for different superconductors with varied pinning landscapes[43–52]. Open and solid symbols indicate the J_c for pristine and superconductors with introduced pinning centers. The inset of Fig. 6 shows J_c vs. J_d for chemical–pressure-controlled Fe-based pnictide Ba122:P films with and without nanoparticles.

regard, it is important to note that although the method for controlling J_d (H_c and λ_{ab}) is different for the cuprate and the pnictide (changing carrier concentration (p) and the chemical pressure (x), respectively), the end result is the same, thus highlighting the general applicability of our strategy.

Further insight into the effects of the combination of increasing J_d and enhancing flux pinning can be obtained from the field dependence of J_c. Figure 7a shows the $J_c(\mathbf{H}||c)$ at 4.2 K for our overdoped (Y,Gd)123 + BHO CC compared with that of several RE123 films and CCs[16,57–59]. As seen for up to 18 T, the $J_c(\mathbf{H}||c)$ of overdoped (Y,Gd)123 + BHO CC is the highest among all superconductors. Compared with overdoped standard Y123 at 5 K[16], the enhancement of our overdoped (Y,Gd)123 + BHO CC is 144% at the self-field and 199% at 5 T. Moreover, compared to that of coherent BHO-doped CCs[59], the $J_c(\mathbf{H}||c)$ of our CC shows a 254% increase at 1 T and 175% increase at 18 T. The remarkable in-field performance of overdoped (Y,Gd)123 + BHO CC is highlighted in Fig. 7b, where the pinning force, $F_p = J_c(H) \times \mu_0 H$, is compared with that of several RE123 materials[16,57–59]. The F_p at 4.2 K of our overdoped (Y,Gd)123 + BHO CC reaches ~3.17 TN/m^3 at 18 T ($\mathbf{H}||c$), which is the highest reported value for any superconductor material. Please note that because the anisotropy of RE123 materials is ~5 (Fig. 5a), the F_p measured along the c axis is the minimum value for a RE123 superconductor.

Conclusions

In summary, we have succeeded in combining this thermodynamic route (increasing J_d by decreasing λ and/or increasing H_c) with our previously developed methods to tailor the size and incorporate large densities of incoherent nanoparticles. We obtain $J_c \sim 150$ MA/cm^2 (~32.4% of J_d) and $J_c \sim 130$ MA/cm^2 (~28.0% of J_d) at 4.2 K and in the self-field for nanocomposite RE123 films on single-crystal substrates and metallic substrates (CCs), respectively. Moreover, for films of chemical–pressure-controlled Ba122:P with incoherent BZO NPs, the $J_c^{s.f.}$ at 4.2 K increases from 1.0 to 8.0 MA/cm^2 due to the increase in J_d in combination with the introduction of high densities of incoherent BZO NPs. To our knowledge, the J_c values attained for our CC of overdoped (Y,Gd)123 in not only the self-field but also the high field are the highest reported to date for any superconductor. This highlights that thermodynamic improvements of superconductors can work in parallel with already successful artificial pinning centers and that a maximum $J_c \sim 0.3\ J_d$ appears to be the current upper limit for the enhancement in J_c.

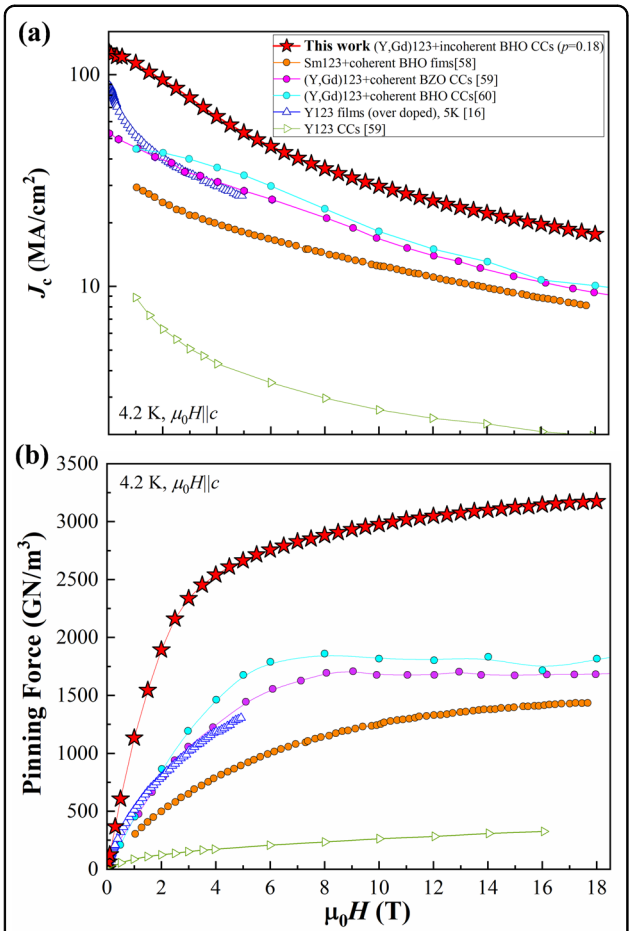

Fig. 7 Critical current density J_c and pinning force F_p as a function of magnetic field. a $J_c(\mathbf{H}||c)$ at 4.2 K and **b** F_p-$\mu_0 H$ curve of overdoped (Y,Gd)123 + BHO CCs at 4.2 K and $\mathbf{H}||c$. For comparison, the data for Sm123 + coherent BHO film[57], (Y,Gd)123 + coherent BZO CC[58], (Y,Gd)123 + coherent BHO CC[59], overdoped Y123 film at 5 K[16], and Y123 CCs[58] are included.

Acknowledgements

This work at Seikei University was supported by JST-FOREST (Grant Number JPMJFR202G, Japan). A part of this work at Seikei University was supported by JSPS KAKENHI (18KK0414 and 20H02184) and Promotion, Mutual Aid Corporation for Private Schools of Japan (Science Research Promotion Fund). This work at Los Alamos National Laboratory was supported by the LDRD office 20210320ER (B.M.) and the US DOE, Office of Basic Energy Sciences, Materials Sciences and Engineering Division (L.C.). This work at AIST was supported by the New Energy and Industrial Technology Development Organization (NEDO). We thank Jeffrey O Willis (LANL) for the helpful discussions and critical reading of the manuscript. M.M. also thanks Akira Ibi for the sample fabrication of PLD-EuBCO films.

Author details

[1]Graduate School of Science and Technology, Seikei University, 3-3-1 Kichijoji-kitamachi, Musashino-shi, Tokyo 180-8633, Japan. [2]Materials Physics and Applications Division, Los Alamos National Laboratory, Los Alamos, NM 87545, USA. [3]JST-FOREST, 7, Gobancho, Chiyoda-ku, Tokyo 102-0076, Japan. [4]Department of Basic Science, The University of Tokyo, Meguro, Tokyo 153-8902, Japan. [5]Department of Electrical and Electronic Engineering, University of Yamanashi, 4-3-11 Takeda, Kofu 400-8511, Japan. [6]Department of Applied Physics, The University of Tokyo, Bunkyo, Tokyo 113-8656, Japan. [7]Nanostructures Research Laboratory, Japan Fine Ceramics Center, 2-4-1 Mutsuno, Atuta-ku, Nagoya 456-8587, Japan. [8]National Institute of Advanced Industrial Science and Technology, 1-2-1 Namiki, Tsukuba, Ibaraki 305-8564, Japan. [9]Institute for Materials Research, Tohoku University, Katahira 2-1-1, Aoba-ku, Sendai 980-8577, Japan

Author contributions

M.M. and B.M. carried out the experimental design. M.M., G.T., and T.H. grew the films and carried out transport measurements. B.M. carried out the data analysis and provided advice and consultation on the flux pinning and manuscript preparation. R.Y. and T.K. carried out microstructural studies. Y.K. carried out the analysis for H_{c2}. T.I. contributed to the discussion on the film preparation. H.K., F.N., and A.M. contributed to the discussion on the penetration depth analysis. K.S. and N.S. carried out the analysis for the resonance frequency. T.O. and S.A. contributed to the discussion on the analysis for the transport measurement at high field. L.C. contributed to the discussion and manuscript preparation. All authors discussed the results and implications and commented on the manuscript. M.M. and B.M. wrote the manuscript with contributions from all the authors.

Competing interests

The authors declare no competing interests.

Publisher's note

Springer Nature remains neutral with regard to jurisdictional claims in published maps and institutional affiliations.

Supplementary information The online version contains supplementary material available at https://doi.org/10.1038/s41427-022-00432-1.

Received: 12 July 2022 Revised: 1 September 2022 Accepted: 6 September 2022.
Published online: 21 October 2022

References

1. Hahn, S. et al. 45.5-tesla direct-current magnetic field generated with a high-temperature superconducting magnet. *Nature* **570**, 496–499 (2019).
2. Wang, Q. et al. Progress of ultra-high-field superconducting magnets in China. *Supercond. Sci. Technol.* **35**, 023001 (2022).
3. Blatter, G., Feigl'man, M. V., Geshkenbein, V. B., Larkin, A. I. & Vinokur, V. M. Vortices in high-temperature superconductors. *Rev. Mod. Phys.* **66**, 1125–1388 (1994).
4. MacManus-Driscoll, J. L. et al. Strongly enhanced current densities in superconducting coated conductors of $YBa_2Cu_3O_{7-x}$+$BaZrO_3$. *Nat. Mater.* **3**, 439–443 (2004).
5. Haugan, T., Barnes, P. N., Wheeler, R., Meisenkothen, F. & Sumption, M. Addition of nanoparticle dispersions to enhance flux pinning of the $YBa_2Cu_3O_{7-x}$ superconductor. *Nature* **430**, 867–870 (2004).
6. Selvamanickam, V., Gharahcheshmeh, M. H., Xu, A., Zhang, Y. & Galstyan, E. Critical current density above 15MAcm^2 at 30K, 3T in 2.2μm thick heavily-doped $(Gd,Y)Ba_2Cu_3O_x$ superconductor tapes. *Supercond. Sci. Technol.* **28**, 072002 (2015).
7. Horide, T., Kametani, F., Yoshioka, S., Kitamura, T. & Matsumoto, K. Structural evolution induced by interfacial lattice mismatch in self-organized $YBa_2Cu_3O_{7-\delta}$ nanocomposite film. *ACS Nano* **11**, 1780–1788 (2017).
8. Miura, M. et al. Strongly enhanced flux pinning in one-step deposition of $BaFe_2(As_{0.66}P_{0.33})_2$ superconductor films with uniformly dispersed $BaZrO_3$ nanoparticles. *Nat. Commun.* **4**, 2499 (2013).
9. Xu, A. et al. J_e(4.2 K, 31.2 T) beyond 1 kA/mm^2 of a ~3.2 μm thick, 20 mol% Zr-added MOCVD REBCO coated conductor. *Sci. Rep.* **7**, 6853 (2017).
10. Sebastian, M. A. P. et al. Study of the flux pinning landscape of YBCO thin films with single and mixed phase additions $BaMO_3$ + Z: M = Hf, Sn, Zr and Z = Y_2O_3, Y211. *IEEE Trans. Appl. Supercond.* **27**, 7500805 (2017).
11. Miura, M. et al. Tuning nanoparticle size for enhanced functionality in perovskite thin films deposited by metal organic deposition. *npg Asia Mater.* **9**, e447 (2017).

12. Li, Z. et al. Control of nanostructure and pinning properties in solution deposited $YBa_2Cu_3O_{7-x}$ nanocomposites with preformed perovskite nanoparticles. *Sci. Rep.* **9**, 5828 (2019).
13. Tinkham, M. *Introduction of Superconductivity* 2nd edn (McGraw-Hill, New York, 1996).
14. Claus, H. et al. Critical current of grain boundaries in YBa_2Cu_3Ox bicrystal films as a function of oxygen concentration. *Phys. Rev. B* **76**, 014529 (2007).
15. Strickland, N. M., Semwal, A., Williams, G. V. M., Verebelyi, D. T. & Zhang, W. Optimizing the doping state of YBCO coated conductors. *Supercond. Sci. Technol.* **17**, S473–S476 (2004).
16. Stangl, A., Palau, A., Deutscher, G., Obradors, X. & Puig, T. Ultra-high critical current densities of superconducting $YBa_2Cu_3O_{7-\delta}$ thin films in the overdoped state. *Sci. Rep.* **11**, 8176 (2021).
17. Sadovskyy, I. A., Koshelev, A. E., Kwok, W., Welp, U. & Glatz, A. Targeted evolution of pinning landscapes for large superconducting critical currents. *Proc. Natl Acad. Sci. USA* **116**, 10291–10296 (2019).
18. Eley, S., Miura, M., Maiorov, B. & Civale, L. Universal lower limit on vortex creep in superconductors. *Nat. Mater.* **16**, 409–413 (2017).
19. Loram, J. W., Mirza, K. A., Liang, W. Y. & Osborne, J. A systematic study of the specific heat anomaly in $La_{2-x}Sr_xCuO_4$. *Phys. C.* **162–164**, 498–499 (1989).
20. Loram, J. W., Mirza, K. A. & Liuet, R. S. Specific heat anomalies in the 108 K superconducting system $Y_{1-x}Ca_xSr_2Cu_2T_{l5}P_{b5}O_7$. *Supercond. Sci. Technol.* **4**, S286 (1991).
21. Niedermayer, C. et al. Muon spin rotation study of the correlation between Tc and ns/m* in overdoped $Tl_2Ba_2CuO_{6+\delta}$. *Phys. Rev. Lett.* **71**, 1764 (1993).
22. Wade, J. M., Loram, J. W., Mirza, K. A., Cooper, J. R. & Tallon, J. L. Electronic specific heat of $Tl_2Ba_2CuO_{6+\delta}$ from 2 K to 300 K for $0 \le \delta \le 0.1$. *J. Supercond.* **7**, 261 (1994).
23. Pereg-Barnea, T. et al. Absolute values of the London penetration depth in $YBa_2Cu_3O_{6+y}$ measured by zero field ESR spectroscopy on Gd doped single crystals. *Phys. Rev. B* **69**, 184513 (2004).
24. Breit, V. et al. Evidence for chain superconductivity in near-stoichiometric YBa_2Cu_3Ox single crystals. *Phys. Rev. B* **52**, R15727(R) (1995).
25. Li, Y. et al. Hole pocket–driven superconductivity and its universal features in the electron-doped cuprates. *Sci. Adv.* **5**, eaap7349 (2019).
26. Kurokawa, H. et al. Relationship between superconductivity and nematicity in $FeSe_{1-x}Te_x$ ($x = 0$—0.5) films studied by complex conductivity measurements. *Phys. Rev. B* **104**, 014505 (2021).
27. Ibi, A. et al. Improvement of in-field performance for EuBCO with heavily doped BHO coated conductors by PLD method with high temperature deposition and low temperature annealing. *IOP Conf. Ser. Mater. Sci. Eng.* **756**, 012024 (2020).
28. Shimoyama, J., Horii, S., Otzschi, K. & Kishio, K. How to optimize critical current performance of RE123 materials by controlling oxygen content. *Mat. Res. Soc. Symp. Proc.* **689**, 265 (2002).
29. Presland, M. R., Tallon, J. L., Buckley, R. G., Liu, R. S. & Flower, N. E. General trends in oxygen stoichiometry effects on Tc in Bi and Tl superconductors. *Phys. C.* **176**, 95–105 (1991).
30. Song, X., Daniels, G. A., Feldmann, D. M., Gurevich, A. & Larbalestier, D. C. Electromagnetic, atomic-structure and chemistry changes induced by Ca-doping of low angle YBCO grain boundaries. *Nat. Mater.* **4**, 470–475 (2005).
31. Sonier, J. E., Brewer, J. H. & Kiefl, R. F. μSR studies of the vortex state in type-II superconductors. *Rev. Mod. Phys.* **72**, 769 (2000).
32. Tallon, J. L. et al. In-Plane anisotropy of the penetration depth due to superconductivity on the Cu-O Chains in $YBa_2Cu_3O_{7-\delta}$, $Y_2Ba_4Cu_7O_{15-\delta}$, and $YBa_2Cu_4O_8$. *Phys. Rev. Lett.* **74**, 1008 (1995).
33. Watanabe, K., Yoshida, K., Aoki, T. & Kohjiro, S. Kinetic inductance of superconducting coplanar waveguides. *Jpn. J. Appl. Phys.* **33**, 5708 (1994).
34. Werthamer, N. R., Helfand, E. & Hohenberg, P. C. Temperature and purity dependence of the superconducting critical field, Hc_2. III. electron spin and spin-orbit effects. *Phys. Rev.* **147**, 295 (1966).
35. Grissonnanche, G. et al. Direct measurement of the upper critical field in cuprate superconductors. *Nat. Commun.* **5**, 3280 (2014).
36. Daumling, M. The reversible magnetization of oxygen deficient $YBa_2Cu_3O_{7-\delta}$. *Phys. C.* **183**, 293–302 (1991).
37. Ramshaw, B. J. et al. Quasiparticle mass enhancement approaching optimal doping in a high-Tc superconductor. *Science* **348**, 317–320 (2015).
38. Zhang, C. et al. Hybrid physical chemical vapor deposition of ultrathin MgB_2 films on MgO substrate with high Tc and Jc. *IEEE Trans. Appl. Supercond.* **23**, 7500204 (2013).
39. Nawaz, S., Arpaia, R., Bauch, T. & Lombardi, F. Approaching the theoretical depairing current in $YBa_2Cu_3O_{7-\delta}$ nanowires. *Phys. C.* **495**, 33–38 (2013).
40. Nawaz, S., Arpaia, R., Lombardi, F. & Bauch, T. Microwave response of superconducting $YBa_2Cu_3O_{7-\delta}$ nanowire bridges sustaining the critical depairing current: evidence of Josephson-like behavior. *Phys. Rev. Lett.* **110**, 167004 (2013).
41. Zhang, C. et al. Fabrication of superconducting nanowires from ultrathin MgB_2 films via focused ion beam milling. *AIP Adv.* **5**, 027139 (2015).
42. Bean, C. P. Magnetization of high-field superconductors. *Rev. Mod. Phys.* **36**, 31–39 (1964).
43. Miura, M. et al. Upward shift of the vortex solid phase in high-temperature superconducting wires through high density nanoparticle addition. *Sci. Rep.* **6**, 20436 (2016).
44. Liang, R., Bonn, D. A. & Hardy, W. N. Evaluation of CuO_2 plane hole doping in $YBa_2Cu_3O_{6+x}$ single crystals. *Phys. Rev. B* **73**, 180505(R) (2006).
45. Nagasao, K., Masui, T. & Tajima, S. Rapid change of electronic anisotropy in overdoped (Y, Ca)$Ba_2Cu_3O_{7-\delta}$. *Phys. C.* **468**, 1188–1191 (2008).
46. Civale, L. et al. Vortex confinement by columnar defects in $YBa_2Cu_3O_7$ crystals: enhanced pinning at high fields and temperatures. *Phys. Rev. Lett.* **67**, 648 (1991).
47. Matsushita, T. et al. Condensation energy density in Bi-2212 superconductors. *Supercond. Sci. Technol.* **19**, 200–205 (2006).
48. Krusin-Elbaum, L., Tsuei, C. C. & Gupta, A. High current densities above 100 K in the high-temperature superconductor $HgBa_2CaCu_2O_{6+\delta}$. *Nature* **373**, 679–681 (1995).
49. Balachandran, S. et al. Beneficial influence of Hf and Zr additions to Nb4at%Ta on the vortex pinning of Nb_3Sn with and without an O source. *Supercond. Sci. Technol.* **32**, 044006 (2019).
50. Tallon, J. L. Thermodynamics and critical current density in high-T_c superconductors. *IEEE Trans. Appl. Supercond.* **25**, 8000806 (2015).
51. Miura, M. et al. Enhanced critical current density in $BaFe_2(As_{0.66}P_{0.33})_2$ nanocomposite superconducting films. *Supercond. Sci. Technol.* **32**, 064005 (2019).
52. Barua, S. et al. Critical current distributions of recent Bi-2212 round wires. *IEEE Trans. Appl. Supercond.* **31**, 6400406 (2021).
53. Gurevich, A. Pinning size effects in critical currents of superconducting films. *Supercond. Sci. Technol.* **20**, S128–S135 (2007).
54. Chaparro, C. et al. Doping dependence of the specific heat of single-crystal $BaFe_2(As_{1-x}P_x)_2$. *Phys. Rev. B* **85**, 184525 (2012).
55. Miura, M. et al. Anisotropy and superconducting properties of $BaFe_2(As_{1-x}P_x)_2$ films with various phosphorus contents. *Appl. Phys. Express* **6**, 093101 (2013).
56. Hashimoto, K. et al. A sharp peak of the zero-temperature penetration depth at optimal composition in $BaFe_2(As_{1-x}P_x)_2$. *Science* **336**, 1554–1557 (2012).
57. Miura, S. et al. Characteristics of high-performance $BaHfO_3$-doped $SmBa_2Cu_3O_y$ superconducting films fabricated with a seed layer and low temperature growth. *Supercond. Sci. Technol.* **28**, 065013 (2015).
58. Xu, A. et al. Strongly enhanced vortex pinning from 4 to 77 K in magnetic fields up to 31 T in 15 mol.% Zr-added (Gd, Y)-Ba-Cu-O superconducting tapes. *APL Mater.* **2**, 046111 (2014).
59. Majkic, G. et al. In-field critical current performance of 4.0 μm thick film REBCO conductor with Hf addition at 4.2 K and fields up to 31.2 T. *Supercond. Sci. Technol.* **33**, 07LT03 (2020).